RESEARCH ARTICLE

WILEY

Aerodynamic performance of a dual turbine concept characterized by a relatively close distance between rotors

Victor Mendoza[1,2] 🄳 | Eirini Katsidoniotaki[2,3] 🄳 | Markos Florentiades[1] | Jorge Dot Fraga[1] | Eduard Dyachuk[1]

[1]Hexicon AB, Stockholm, Sweden

[2]Division of Electricity, Uppsala University, Uppsala, Sweden

[3]Centre of Natural Hazards and Disaster Science (CNDS), Uppsala, Sweden

Correspondence
Victor Mendoza, Hexicon AB, Östra Järnvägsgatan 27, Stockholm 111 20, Sweden.
Email: victor.mendoza@hexicongroup.com

Abstract

In this work, a closely spaced dual turbine concept is studied. The distance between the two side-by-side hubs is 1.05D, where D is the rotor diameter. This configuration has a potential benefit for offshore wind developments in which power density can be maximized. The main goal is to evaluate the overall aerodynamic performance, blade loads, and wake structure of a reference wind turbine generator operating within this dual turbine configuration and to compare the effects against those for the typical single turbine configuration. For this purpose, an actuator line model has been employed together with the large eddy simulation approach for predicting the turbulence effects. This model was implemented by using the open-source computational fluid dynamics toolbox OpenFOAM. Results show a better performance for the dual turbine concept. Under same operating conditions, the aerodynamic power of each turbine within the dual concept is higher than the power of the stand alone turbine, particularly at lower operating wind speeds (approximately 2% to 3% of extra power per turbine). Comparison between the two configurations shows similar character of the tangential and normal forces acting on the blades in terms of magnitude and fluctuation, eliminating potential concerns regarding fatigue and blade design. The largest difference in the tangential and normal root bending moments are approximately 3% and 2%, respectively, between single and dual turbine configurations. Finally, wake recovery analysis shows a downwind velocity deficit that is not enhanced streamwise in the dual turbine configuration with no considerable difference after 7D.

KEYWORDS
actuator line model (ALM), dual turbine configuration, horizontal axis wind turbine (HAWT), large eddy simulation (LES)

1 | INTRODUCTION

There is high demand for electricity produced by renewable energy resources. Developers of wind farms are increasingly interested in harnessing offshore wind energy resources due to the multiple advantages; among others, the offshore wind speeds are faster and steadier than onshore, enabling a more stable energy production. The newest wind turbines are technologically advanced and include engineering and mechanical

innovations to maximize the efficiency and increase the electricity production for a longer lifetime. Globally turbines continue to grow in capacity, hub height, and rotor diameter, which decreases overall project costs.[1-3] However, this energy transition presents some technical, scientific, and legal challenges that need to be overcome.

The identification of the wind farm layout is an important stage during the design process of the farm. A common approach in the wind industry consists of a multiobjective optimization process that considers technical, commercial, environmental, political, and social variables to conduct the micrositing assessment. From a purely technical perspective, wind farm energy production is highly influenced by the distance between the turbines; this dictates the levels of wake interference, which is a major source of aerodynamic loss.[4] This is an undesirable effect that occurs when turbines are located close to each other and operate within the wake created by the upwind turbine. These wake structures result in a velocity deficit and higher turbulence, reducing the energy production of the wind farm and increasing the blade loads on the downwind turbines. In this scenario, novel multirotor (and multiturbine) concepts have been developed, aiming to improve the performance of wind farms through increasing the power density while reducing number of platforms and costs associated to cable layout and cable efficiency. In 2016, Vestas Wind Energy Systems A/S developed and built a multirotor wind turbine demonstrator located in the Technical University of Denmark (DTU), Campus Risø, which consists of four rotors arranged in both top and bottom pairs.[5-7] Pelagic Power AS designed the concept of W2Power, a floating platform for combined extraction of Wind & Wave energy, accommodating two standard offshore wind turbines.[8] Similarly, Flowocean AB developed the FLOW concept, which uses two turbines on the same platform.[9] These concepts are shown in Figure 1.

To evaluate the viability of the multirotors concepts, it is necessary to have a fundamental knowledge about the flow phenomena involved, aerodynamic performances, blade loads, and wake structures. Hence, both measurements and numerical simulations are essential for the achievement of this purpose. Paul van der Laan et al. performed numerical simulations for the Vestas multirotor demonstrator, and these results were compared against field measurements[5] showing an increase in aerodynamic power below the rated wind speed of 1.8% as well as a shorter wake recovery process than a single rotor wind turbine with an equivalent rotor diameter. Chasapogiannis et al[10] employed both actuator disk with computational fluid dynamics (CFD) solvers and vortex method to analyze a multirotor wind turbine with seven rotors. Both numerical approaches predicted a power increase of around 3%. In Hebbar et al,[6] a multirotor system (four rotors) was analyzed using the actuator line model (ALM) approach for studying its wake recovery process showing a early onset when compared to a single rotor simulation. Van der Laan et al. predicted an increase in the annual energy production (AEP) of of 0.3%–1.7%[11] in a wind farm array with 4 × 4 (16 turbines) arrangement with four rotor units compared to the same array employing single rotor units with equivalent diameter. Bastankhah et al. found that the wake of a four-rotor system at greater distances than 5–8 rotors diameters converge into a form of a single wake.[12]

As an additional contribution into the understanding of multirotor concepts, this work studies the performance of a dual turbine concept characterized by a horizontal distance between the hubs of $1.05D$, where D is the rotor diameter. This configuration aims to represent Hexicon's TwinWind technology, a patented floating foundation that hosts two wind turbines with inclined towers (as shown in Figure 2). The TwinWind is a downwind semisubmersible platform with a single-point mooring system at which the floating platform passively aligns with the wind direction. The floater has a triangular truss structure and three columns on the vertices. Two of the columns support two inclined towers while the third column hosts the mooring connection and a passive weathervaning system. The TwinWind configuration is further referred to as a "dual turbine" configuration.

The present work provides results of the aerodynamic performance, blade loads, and wake structure when a reference wind turbine generator (WTG) is operating in both single and dual turbine configurations. The main goal is to evaluate the effects (potential benefits and drawbacks) of the presented dual turbine concept compared against the conventional concept with a single turbine. For this purpose, an ALM has been employed using the open-source CFD toolbox OpenFOAM to solve the governing equations and to calculate the resulting flow. The IEA 10-MW offshore wind turbine[13] was considered as a reference turbine. For the aerodynamic performance analysis, both turbine configurations have been tested over a wide range of wind velocities in order to investigate the resulting power and thrust of the reference turbine over different operating regimes (below, at and above the rated wind speed) and configurations. The same configurations and wind conditions were considered for the blade loads analysis, in which the resulting averaged normal and tangential forces on one blade have been studied over one whole rotor

FIGURE 1 Multirotor concepts developed by Vestas[5] (left), W2Power[8] (center) and Flowocean[9] (right).

FIGURE 2 Schematic of Hexicon's floating platform with the dual turbine concept.

revolution. For the wake structure analysis, the wake behind the single and dual turbine configurations was assessed at different distances downstream. In all the performed case studies, a uniform wind has been used as the inflow condition.

This paper is organized as follows: Section 2 provides further information about the principal methodology for the analysis and detailed description of the dual turbine concept. In Section 3, the numerical model is verified and validated based on the design data of the power and thrust curves available in the IEA report.[13] In Section 4, the results are presented and discussed, and in Section 5, the conclusions of this study are highlighted.

2 | METHODOLOGY

2.1 | The ALM

The ALM is a time-dependent model based on the classic blade element momentum (BEM) theory. This three-dimensional model was developed by Sørensen and Shen,[14] and it is commonly employed to study the flow field around both horizontal and vertical axis wind turbines. In the ALM, the blade is approximated as a force distribution along the blade span by using n-elements, which have the aerodynamic behavior of two-dimensional airfoil profiles. Both tangential and normal forces are calculated by using a dynamic stall model (DSM) commonly based on empirical data; however, in the present work, the DSM has not been employed. Compared to the traditional full-body solved CFD modeling, the ALM removes the need to solve the governing equations in local highly refined mesh regions around the blade boundary layer, and therefore considerably reduces the computational cost. The presented work is focused on the analysis of the aerodynamic performance of the dual turbine configuration, blade loads and overall wake structure. The library turbinesFoam developed by Bachant et al[15–17] has been employed for the implementation of the ALM. This model has been previously validated by Mendoza et al. for both horizontal and vertical axis wind turbines,[4,18–22] by using measurements of power coefficients C_P, thrust coefficients C_T, blade loads, and wake velocity in representative sections. Additionally, the employed ALM has been used in a wide range of operational conditions such as single or interacting turbines, inside wind tunnels, or at open sites, within a uniform flow or a neutral atmospheric boundary layer, and so forth.

The large eddy simulation (LES) approach based on an incompressible fluid case is considered for predicting the turbulence effects, and therefore, the governing Navier–Stokes equations can be expressed as

$$\frac{\partial \tilde{u}_i}{\partial x_i} = 0 \tag{1}$$

$$\frac{\partial \tilde{u}_i}{\partial t} + \frac{\partial \tilde{u}_i \tilde{u}_j}{\partial x_j} = -\frac{1}{\rho}\frac{\partial \tilde{p}}{\partial x_i} + \nu \frac{\partial^2 \tilde{u}_i}{\partial x_j \partial x_j} - \frac{f_i}{\rho} - \frac{\partial \tau_{ij}}{\partial x_j} \tag{2}$$

where $\tilde{u}_i$ and $\tilde{p}$ correspond to the velocity and pressure grid-filtered values, respectively. ν represent the the kinematic viscosity, f_i the acting body forces (blade), and τ_{ij} the subgrid scale (SGS) stress defined as $\tau_{ij} = \widetilde{u_i u_j} - \tilde{u}_i \tilde{u}_j$. To parameterize the deviatoric part of the SGS stress, the Smagorinsky model[23] was used as

$$\tau_{ij} - \frac{1}{3}\delta_{ij}\tau_{kk} = -2(C_S \tilde{\Delta})^2 |\tilde{S}| \tag{3}$$

where $\tilde{S}_{ij} = \frac{1}{2}\left(\frac{\partial \tilde{u}_i}{\partial x_j} + \frac{\partial \tilde{u}_j}{\partial x_i}\right)$ is the resolved rate-of-strain tensor, $\tilde{\Delta}$ is the grid size, and $C_S = 0.1667$ the Smagorinsky constant (usually it has a value between 0.1 and 0.2).

The employed lift and drag coefficients (C_L and C_D, respectively) implemented into the ALM are taken from the IEA report.[13] First, the ALM samples the local flow velocity for each blade element, providing the angle of attack α and relative velocity $\vec{V}_{rel}$. These terms are calculated by using the geometrical relation between the blade rotational velocity $\vec{V}_{blade} = -\Omega r$, where Ω represents the angular velocity of the rotor and r its radius, and the incoming flow velocity $\vec{V}_{in}$, which is normally smaller than the free-stream flow velocity $\vec{V}_\infty$ through the following equation:

$$\vec{V}_{rel} = \vec{V}_{in} - \vec{V}_{blade} \tag{4}$$

The relative wind angle (typically referred to as the inflow angle) is represented by the sum of the angle of attack, pitch angle, and blade twist angle $\varphi = \alpha + \gamma + \beta$. A common practice is to consider $\vec{V}_{in}$ at the location of the element; however, in this work, this has been defined by calculating the average velocity from a defined number of samples around the element and which is axi-symmetrically distributed around the quarter position on the profile plane. The force coefficients are linearly interpolated from a table as a function of the local angle of attack, and the ALM imparts them back into the flow solver as body forces. The velocities and forces on a blade cross-section for one element are displayed in Figure 3.

Once α and $\vec{V}_{rel}$ are obtained (removing the spanwise component for the latest), the lift and drag forces per spanwise length unit can be calculated as

$$F_L = \frac{1}{2}\rho c C_L |\vec{V}_{rel}|^2 \tag{5}$$

$$F_D = \frac{1}{2}\rho c C_D |\vec{V}_{rel}|^2 \tag{6}$$

where C_L, C_D, ρ, and c correspond to the drag coefficient, lift coefficient, wind density, and local chord length, respectively. The direction of the lift force is projected perpendicular to $\vec{V}_{rel}$ and the blade span direction while the drag force is projected in the direction of the relative velocity. Once all the actuator element forces are calculated, they are integrated as body source forces per unit of density into Equation (2) for the momentum conservation. The extracted power of a wind turbine can be expressed in terms of the torque as

$$P = Q\Omega \tag{7}$$

with Q as the turbine torque and Ω the rotational speed of the rotor. The tangential force F_T is directly related to the turbine torque within one revolution as

$$Q = \int_{blade\ root}^{blade\ tip} N_B r(s)\langle F_T(s)\rangle ds \tag{8}$$

where N_B denotes the number of blades, r the radius of the turbine, and $\langle F_T \rangle$ the averaged tangential force between the three blades.
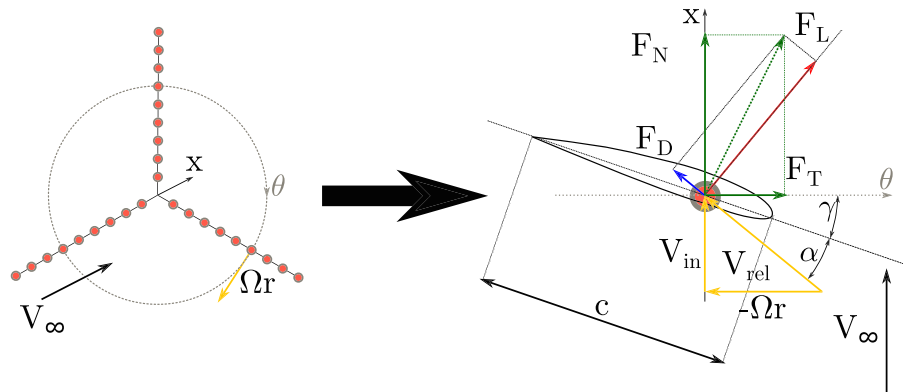

FIGURE 3 Schematic of the velocities and forces in a blade cross-section for one element (with $\beta = 0°$).

In order to avoid numerical instabilities caused by large gradients, the calculated forces by the ALM have been smoothly dispersed on several mesh cells. The obtained source term forces are projected around the position of the elements by considering a three-dimensional Gaussian kernel. A projection function η is employed for this purpose, and which is multiplied by the local force obtained from from the actuator line element and transmitted to the cell with a distance $|\vec{d}|$ from the quarter chord location. This can be expressed as

$$\eta = \frac{1}{\epsilon^3 \pi^{3/2}} \exp\left[-\left(\frac{|\vec{d}|}{\epsilon}\right)^2\right] \tag{9}$$

where ϵ represents a smoothing width parameter and which is chosen as the maximum value between three different contributions related to a quarter of chord length, the mesh size, and the momentum thickness produced by drag forces

$$\epsilon = \max\left[\frac{c}{4}, 4\sqrt[3]{V_{\text{cell}}}, \frac{cC_D}{2}\right] \tag{10}$$

with V_{cell} corresponding to the cell volume. Glauert corrections were considered for the end effects.[24] Further details about the force projection can be found in Bachant et al.[16]

2.2 | Reference wind turbine IEA 10-MW

The 10-MW offshore reference wind turbine developed within the IEA Wind Task 37[13] has been chosen for the validation of the model and evaluation of the dual turbine concept. This turbine has three blades and a rotor diameter of $D = 198$ m, its main characteristics are denoted in Table 1. The details of the blade cross-sections and other aerodynamic properties can be found in the technical report for the IEA Wind Task 37.[13]

This work targets to isolate the inherent effects produced by the dual turbine configuration; thus, rigid aerodynamic simulations have been considered to represent the rotor.

2.3 | TwinWind—Hexicon's dual turbine concept

The dual turbine concept developed by Hexicon is characterized by a floating foundation, which hosts two wind turbines with relatively close separation of $1.05D$ between the turbine rotors (hub to hub) and weathervanes around its single point mooring system located in front column, upwind of the turbines. This design specifically allows the foundation, rather than the individual turbine nacelles, to align with the wind direction. This innovative design allows for the deployment of more turbines per sea area, increasing the energy yield per acreage and reducing the environmental impact. This concept also mitigates the total costs of cabling, steel, installations, and maintenance.[25]

TABLE 1 Main characteristics of the IEA 10-MW reference wind turbine.

Item	Unit	Value
Number of blades		3
Rotor diameter	m	198
Hub diameter	m	4
Hub height	m	122
Cut-in, rated and cut-out wind speed	m/s	4, 11 and 25
Rated electrical power	MW	10
Minimum and maximum rotor speed	rpm	6.0 and 8.68
Maximum tip speed	m/s	90
Tilt angle	°	6
Cone angle	°	−4

3 | NUMERICAL MODEL SETUP

A Cartesian coordinate system has been implemented with its origin at the center of the turbine rotor blade plane and in the middle point between rotors for the single and dual turbine configurations, respectively. The x-axis has a positive value in the direction of the free stream flow. The turbines are rotating in the clockwise direction. The geometry of the turbine considered in this study includes the blades and hub as well as the rotor tilt angle.

The computational domain has a dimension of $L_x \times L_y \times L_z$, with L_x representing the length (free-stream flow direction), L_y the width and L_z the height of the domain, respectively. The turbine rotor plane has been located in the center of the domain with an offset of 5D toward the inlet of the domain. A uniform hexahedral cell distribution (with orthogonal cells and aspect ratio equal to 1) has been employed as the mesh topology for the whole domain discretization.

Refinement regions $n = 3$ and $n = 2$ have rectangular cuboid geometry, with z-dimension of 2.0D and 3.0D, respectively. Note that z-dimension of the refinement regions $n = 3$ and $n = 2$ is equal for domains with dual and single turbine configurations. The finest refinement region, $n = 4$, is a cylinder with diameter of 1.3D and height of 1.26D as shown in Figure 4. For the dual turbine configuration, two cylinders are considered, which are concentric with the axis of the rotors (one per turbine). Every refinement covers a distance of 0.5D in the upwind direction of the rotor. For the dual turbine configuration, the employed turbines are further denoted as T_1 and T_2, and they are located in the positive and negative direction of the y-axis, respectively. The blades of T_1 and T_2 rotate synchronously with an azimuthal angle equal to $0°$ pointing into the positive z-axis direction, and with a clockwise rotation when seeing from the incoming flow direction as shown in Figure 5.
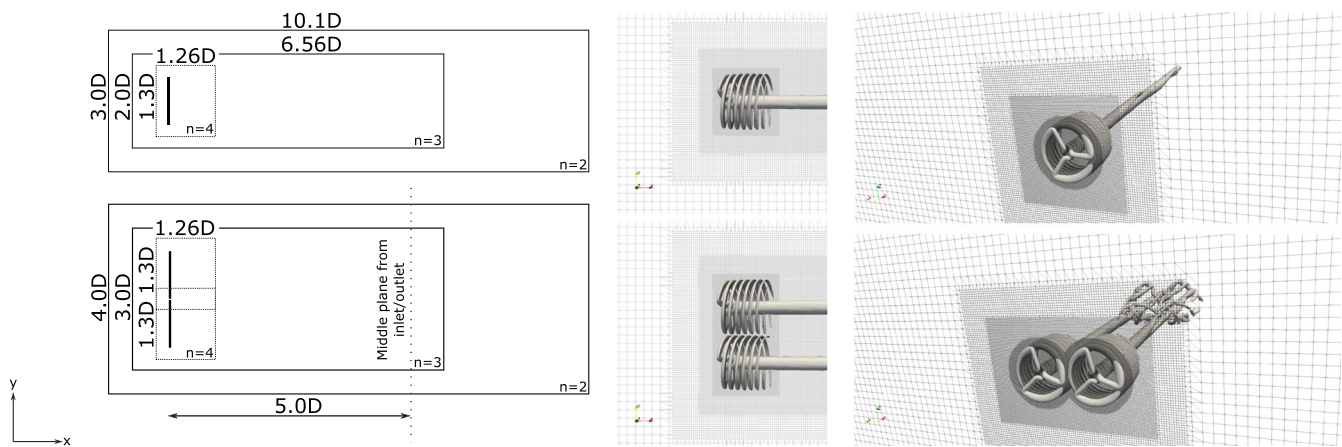

FIGURE 4 Mesh refinement regions for both single and dual turbine configurations: dimensions on the horizontal middle plane (left), and zoomed views from the top (center) and in perspective (right).
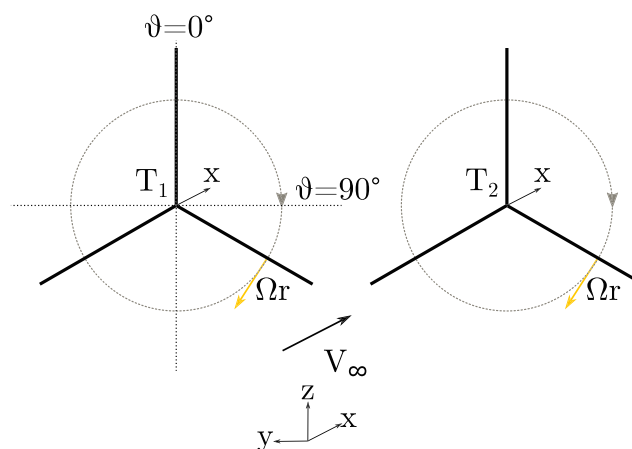

FIGURE 5 Schematic of the blade angles and rotating motion for the dual turbine configuration.

3.1 | Model verification

In order to establish both the resolution and domain size requirements for the grid employed together with the ALM, a parametric study of their influence on the obtained results has been conducted. A slip velocity condition has been treated at the lateral walls of the domain with a uniform inflow wind speed at the inlet of $V_\infty = 11.4$ m/s (rated wind speed), for all the cases.

3.1.1 | Grid convergence study

The increasing use of CFD codes for practical applications of complex flows creates the requirement to examine the accuracy of the results. It is important to verify the numerical errors and/or the uncertainty of a simulation, in order to understand how the final solution is affected. The solution verification entails the estimation of the numerical error and/or uncertainty of a given simulation, yet the exact solution is not known. According to Roache,[26] the discretization error is one of the most critical numerical errors encountered in CFD simulations and occurs due to the representation of the governing flow equations and other physical models as a system of algebraic equations in a discrete domain of space and time. The spatial discretization numerical error depends on the computational grid quality and size, and the CFD solution becomes less sensitive to this error as the grid is refined. In practical engineering problems, the asymptotic range convergence is difficult to be achieved.

In the present study, an uncertainty estimation[27] is implemented when reporting the results of the grid convergence study, which accepts the practical limitations in grid size. The spatial discretization error is estimated from a power series and the least-squares approach is implemented for fitting the CFD data to these expansions. The error estimate is converted to an estimate of the uncertainty, U_ϕ, which indicates the error interval on how far the solution is from the asymptotic value, that is, how much the solution will change with a further grid refinement.

The size of the domain for this study is $15.25D \times 12.62D \times 12.62$, for L_x, L_y, and L_z, respectively, and it is uniformly divided into N_x, N_y, and N_z grid points. Four rotor cell sizes Δx_{rotor} were examined with a constant grid size ratio between them, which is approximately equal to $\sqrt{2}$. The objective of the analysis is to determine the power output (in form of power coefficient, C_P) from the single rotor wind turbine at normal operational condition at rated wind speed, and the influence of the cell size on it. The rotor cell size for the finest refinement area and the results of the spatial discretization study are presented in Table 2 and Figure 6. Monotonic convergence is found and the uncertainty values for the power output is less than 2.5% for all the examined cases, particularly for the two finer ones where the uncertainty is lower than 1%.

TABLE 2 Results of the spatial discretization study.

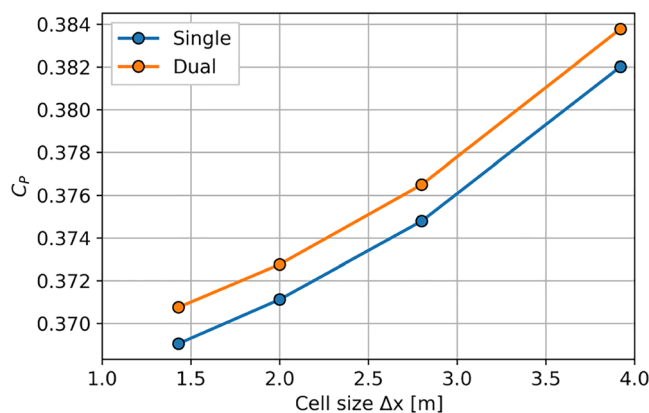| Case	N_x	N_y	N_z	Δx_{rotor} [m]	Total cells [-] (single)	U_ϕ [%] (single)	Total cells [-] (dual)	U_ϕ [%] (dual)
1	48	40	40	3.92	862,508	2.34	1,272,064	2.32
2	68	56	56	2.80	2,299,276	1.44	3,507,392	1.41
3	95	78	78	2.00	6,338,385	0.98	9,582,948	0.95
4	133	109	109	1.43	17,074,288	0.72	25,925,200	0.70

FIGURE 6 Power coefficient for the last 10 revolutions when varying the rotor cell size.

In Figure 6, it is shown that the drop of C_P decreases when increasing the grid resolution, and therefore, the difference in the obtained value begins to be stable. Considering the relation between numerical accuracy and computational cost, the mesh topology with $\Delta x_{rotor} = 2$ m (Case 3) should be high enough taking into account an uncertainty value U_ϕ lower than 1%, and therefore, it is employed for the subsequent studies.

3.1.2 | Numerical domain sizing

The size of the computational domain (width and length) needs to be properly characterized in order to eliminate the side-walls effects, furthermore, the domain must be large enough in order to avoid any influence from the boundaries on the flow around and behind the turbine. A study considering four different widths and lengths was conducted, where the examined variation were increased by a factor of approximately $\sqrt{2}$. For every domain variation, the width is kept the same as the height ($L_y = L_z$). Both cases with single and dual turbine configuration has been investigated. Figure 7 exhibits the induction zone when varying the dimensions of the domain, showing that the induction zone size is not affected by these variations.

The effects on the power output were compared through the root mean square error (RMSE), using as reference case both the larger width and length of the domain. The resulting RMSE values are listed in Table 3.

It can be observed that the effects from both the side walls and domain length are relatively small since the RMSE values are lower than 0.020530% in all cases. Considering the RMSE and accounting for computational cost, the 12.62D width and length of 35D are selected for characterizing the domain size in the further studies. Figure 8 reveals the variation of the power coefficient C_P as function of both width and length of the domain. It is shown that larger domain dimensions than the studied ones will not produce a relevant differentiation on the obtained results. As explained in Section 3.1.1, this study has been performed considering a mesh size of $\Delta x = 2$ m in the region with highest refinement (around the rotor).

3.2 | Model validation

The employed ALM has been validated against the rotor steady state operational data from simulations on the IEA technical report in Bortolotti et al.[13] The IEA analysis has been computed using HAWCStab2 including deflections.[28] The validation is focused on the representation of the
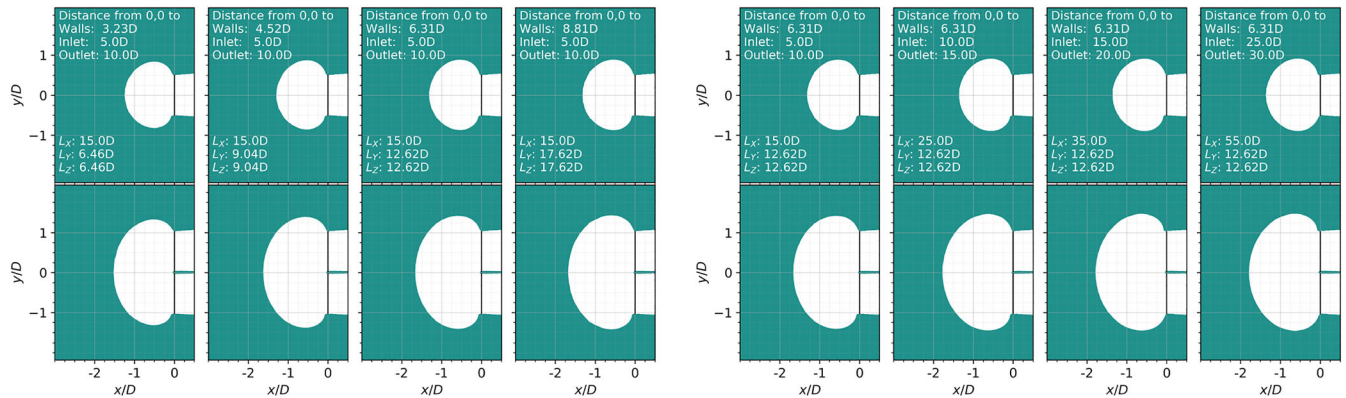

FIGURE 7 Induction zones when varying the width L_y (left) and length L_x of the domain. Colored zones represent normalized wind speed values higher than 1.

TABLE 3 Results of the numerical domain sizing studies.

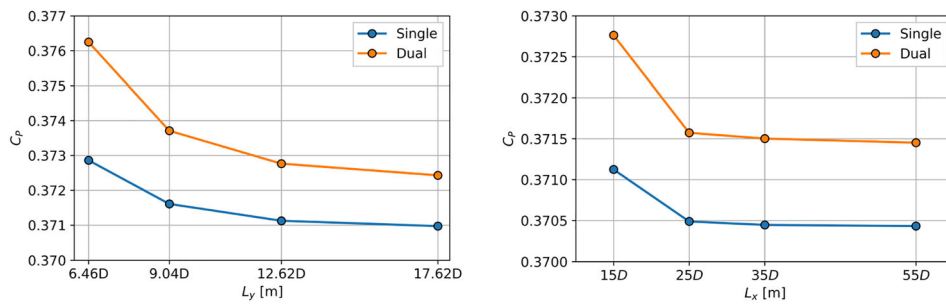| Case	L_y (=L_z) [m]	RMSE (single) [%]	RMSE (dual) [%]	Case	L_x [m]	RMSE (single) [%]	RMSE (dual) [%]
1	6.46D	0.010160	0.020530	1	15D	0.003721	0.007054
2	9.04D	0.003424	0.006881	2	25D	0.000306	0.000656
3	12.62D	0.000835	0.001801	3	35D	0.000215	0.000246
4	17.62D	-	-	4	55D	-	-

FIGURE 8 Averaged power coefficient C_P for the last 10 simulated revolutions when varying the width L_y (left) and length L_x of the domain.
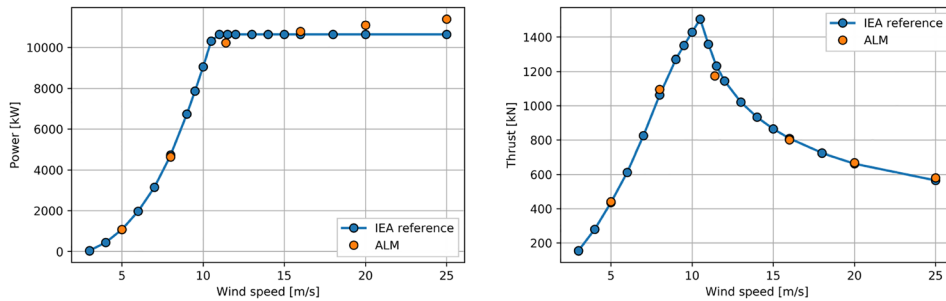

FIGURE 9 Aerodynamic power and thrust for for the 10-MW reference turbine at different wind speeds.

aerodynamic performance of the turbine characterized by the power and thrust as function of the inflow wind speed. The results are depicted in Figure 9, and they show a satisfactory agreement between the numerical results and the reference data, with some discrepancies in the power prediction at high wind speeds (overestimation). This can be produced, among others, because the employed model does not consider some relevant design variables like aeroelastic blade properties and cone angle, which are implemented in the IEA simulations.

4 | RESULTS AND DISCUSSIONS

The simulations have been run for at least 50 rotor revolutions to reach convergence of aerodynamic power.

4.1 | Aerodynamic power and thrust

Figure 10 illustrates specific values for the isosurfaces of both, the Q-criterion, and the normalized streamwise velocity component U_x/V_∞. The Q-criterion can be defined as the fluid regions with a positive second invariant of the velocity gradient tensor, and it is used as a good indicator of turbulent flow structures (produced wake). The normalized streamwise velocity component is employed to identify and quantify regions with accelerated flow compared to the free-stream flow velocity ($U_x/V_\infty = 1$). A flow acceleration region is observed at the interface between the rotors for the dual configuration, which is not present in the case of the single turbine configuration (for the chosen values of accelerated flow). This effect is more pronounced at lower speeds, and it is likely the cause of the additional power and thrust obtained by the reference turbine when it operates in the dual configuration. Since higher speed flows are produced between and around the rotors (jet effect), there is a larger kinetic energy available for power production.

The averaged power and thrust over the last 10 revolutions have been compared between the single turbine configuration and the two turbines in the dual configuration. These results have been computed over a wide range of operating conditions with $V_\infty = 5,8, 11.4, 16, 20$, and 25 m/s, and they are shown in Table 4. There is an increase in both power and thrust for the dual configuration turbines, particularly at lower wind speeds. For both power and thrust, the difference between single and dual configuration is less for wind speeds higher than the rated one ($V_\infty = 11.4$ m/s). With the implementation of a controller, the pitch angle would be regulated above rated wind speed to reach the same rated
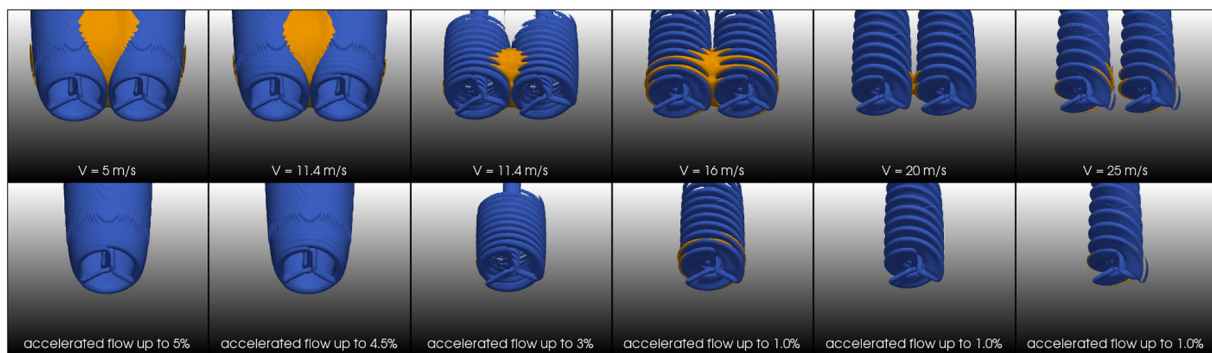
FIGURE 10   Isosurfaces of the normalized streamwise velocity component (orange) and Q-values of 0.0001 (blue) for different wind speeds in both single and dual turbine configuration.

TABLE 4   Aerodynamic performance of the reference wind turbine for different wind speeds in both single and dual turbine configuration.

Wind speed [m/s]	5	8	11.4	16	20	25
Power single [kW]	1071.45	4634.50	10224.60	10780.99	11090.26	11391.49
Power dual T_1 [kW]	1104.51	4739.33	10252.83	10790.79	11095.28	11393.44
Power dual T_2 [kW]	1102.90	4732.87	10247.70	10789.43	11094.97	11393.71
Extra power T_1 [%]	3.08	2.26	0.28	0.09	0.05	0.02
Extra power T_2 [%]	2.93	2.12	0.23	0.08	0.04	0.02
Thrust single [kW]	440.39	1095.28	1174.43	800.23	668.59	579.97
Thrust dual T_1 [kW]	444.99	1103.97	1176.17	800.75	668.82	580.04
Thrust dual T_2 [kW]	444.76	1103.44	1175.81	800.66	668.79	580.05
Extra thrust T_1 [%]	1.04	0.79	0.15	0.06	0.03	0.01
Extra thrust T_2 [%]	0.99	0.75	0.12	0.05	0.03	0.01

power in the single and dual rotor configurations. In terms of the generated power by T_1 and T_2 in the dual configuration, their largest difference is in the order of 10 kW, which is 0.1% of the rated power of the reference turbine (10 MW), and therefore, it can be considered as negligible.

The largest extra power occurs at 5-m/s wind speed, where the power increase between the dual turbines and the single turbine is 3.08% and 2.93%.

4.2 | Blade loads

The analysis of tangential and normal blade forces acting on the turbine rotor has been performed for the reference turbine operating in both single and dual turbine configurations. The tangential force is related to the produced power while the normal force is related to the rotor thrust and the losses of kinetic energy of the flow. The understanding of these forces is essential for an appropriate rotor design. The average root bending moment fluctuations for one blade over the last 10 revolutions are investigated in order to identify additional forces on the blades which could appear as a response to the operation on the dual turbine configuration. The results are depicted in Figure 11 showing the magnitude of the tangential (torque component) and normal root bending moments (rbm_T and rbm_N, respectively).

Asymmetric behavior is observed on both tangential and normal root bending moments around one revolution, which can be produced due to the tilt angle of the rotor considered for the simulations. For the studied wind speeds, there are increased root bending moment fluctuations of the dual configuration compared to the single one, particularly at lower wind speeds. For the tangential bending moments, larger magnitudes and differences are noticed within the blade position before and after 180° for T_1 and T_2, respectively. For the normal forces, when the blades are closest, they get the highest impact (peaks of magnitude) of among others accelerated flow, which might be experienced around 90° and 270° for T_1 and T_2, respectively. In general, the root bending moment magnitudes are higher over one revolution when operating in the dual turbine configuration. Root bending moment differences are almost negligible at high wind speeds. This is consistent with
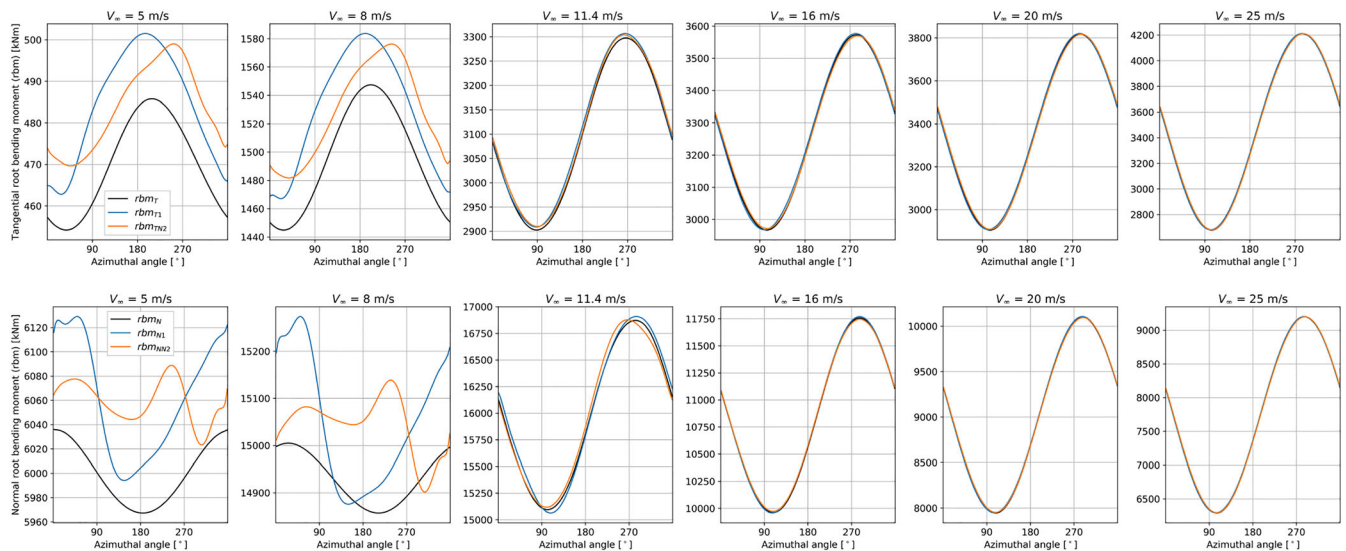
FIGURE 11 Tangential (top) and normal (bottom) root bending moments on one blade at different wind speeds for the last ten revolutions.

the results in Figure 10 and Table 4 regarding flow acceleration between and around the two rotors, and which can be a reason for the power increase.

The tangential root bending moment increases with wind speed and thus more power is being generated. However, above the rated wind speed, the rotational velocity of the rotor is maintained constant, resulting in some further increases in the tangential root bending moments. The magnitude of the normal root bending moment increases with increased wind speed until the rated wind speed and decreases for wind speeds higher than the rated wind speed (due to the blade pitch). The largest difference of the tangential root bending moment is approximately 3%, whereas the normal root bending moment difference is less than 2% when comparing single and dual turbine configurations. These higher differences occur at lower wind speeds and then become negligible at wind speeds higher than the rated one.

Figures 12 and 13 show tangential and normal forces per blade length. For the tangential forces, the larger loads are distributed along the blade during entire revolution at lower wind speeds, but these loads are concentrated on the region close to the blade root below the rated wind speed. For the normal forces, the larger loads are concentrated near the blade tip at lower wind speeds, and these move toward the blade root as wind speed increases. Noticeable additional forces appear along the blade under the rated wind speeds for the dual turbine configuration, particularly in the region between the rotors.

4.3 | Wake structure

Figure 14 and 15 show the normalized streamwise velocity component U_x/V_∞ in the horizontal middle plane and at different representative sections perpendicular to the main flow located behind the rotors plane ($x/D = 0$), respectively. This allows for the analysis of the resulting wake's overall structure (location, shape and extension), and additionally, to investigate the wake recovery process for both turbine configurations, identifying similarities and discrepancies. In both single and dual turbine configurations, the wake structure is not fully symmetric. The dual configuration is characterized by a larger induction zone in front of the rotors which has a length of around 1.75D in the negative x-axis direction, and is considered far from the domain inlet as shown in Figure 7. This induction zone is the consequence of the pressure field due to the presence of a structure. This in turn disturbs the wind field in front of the turbine rotors. In addition, it is shown that the flow disturbance is significantly enhanced by the presence of a second closely-spaced turbine. As discussed before, there is a larger flow acceleration zone around and in between the rotors. For the dual turbine configuration, the resulting wake covers a wider region in both the cross-stream y-axis and the vertical z-axis directions.

In order to perform a quantitative comparison of the wake produced by the different turbine configurations, the horizontal profiles of the normalized streamwise velocity component at different representative downstream sections are also depicted in Figure 14. At the near-rotor sections, the wake produced by the dual rotor is characterized by a larger velocity deficit. In this region, both configurations show an irregular deficit profile influenced by the hub (single turbine configuration) and the distance between the two hubs (dual turbine configuration). The irregular profile dissipates downstream and smoothly transitions toward a Gaussian profile. The differences between the magnitude of velocity deficit in both
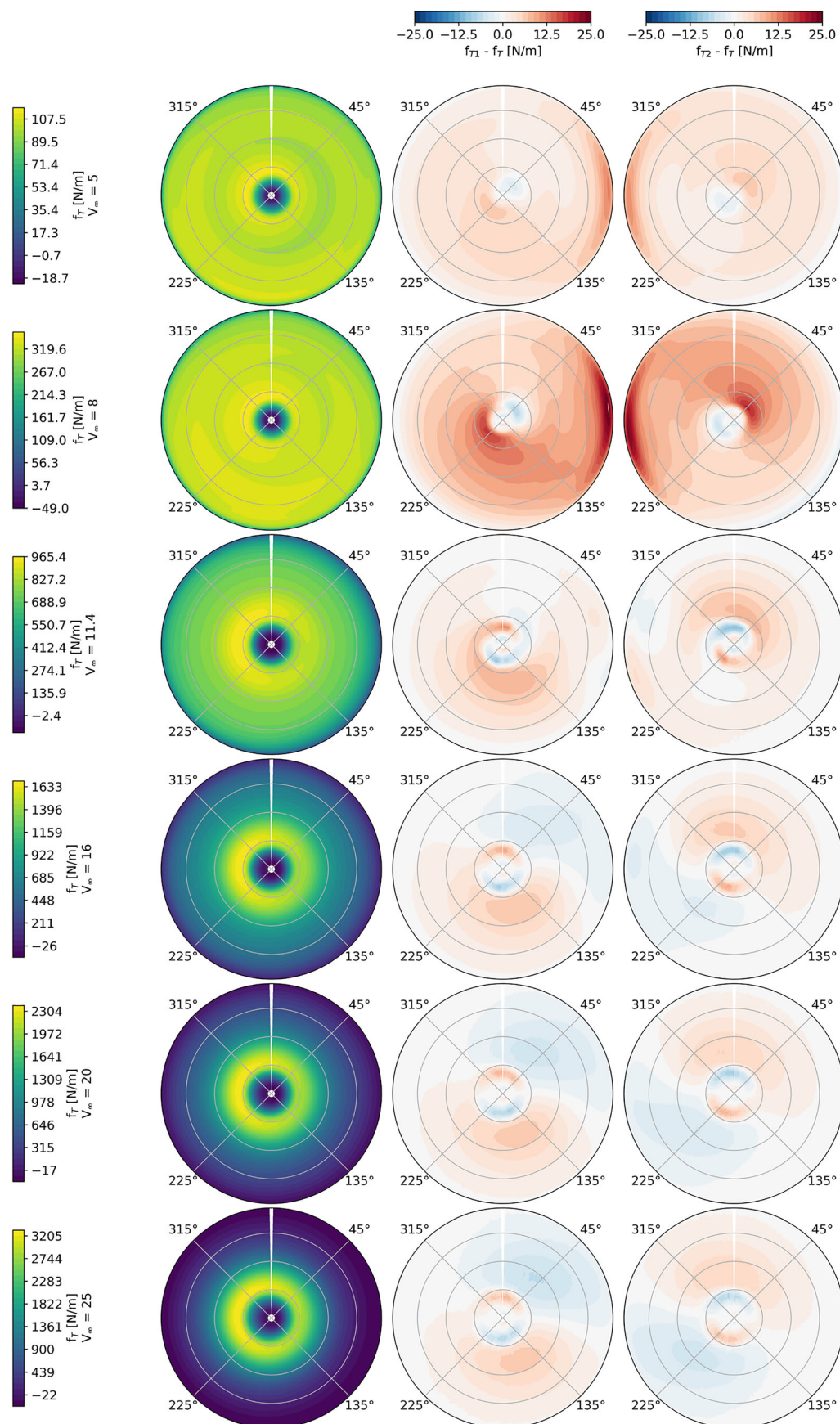
FIGURE 12 Tangential forces per blade length for single configuration f_T (viridis) and its variation for the dual turbine configuration (blue/red) at different wind speeds.
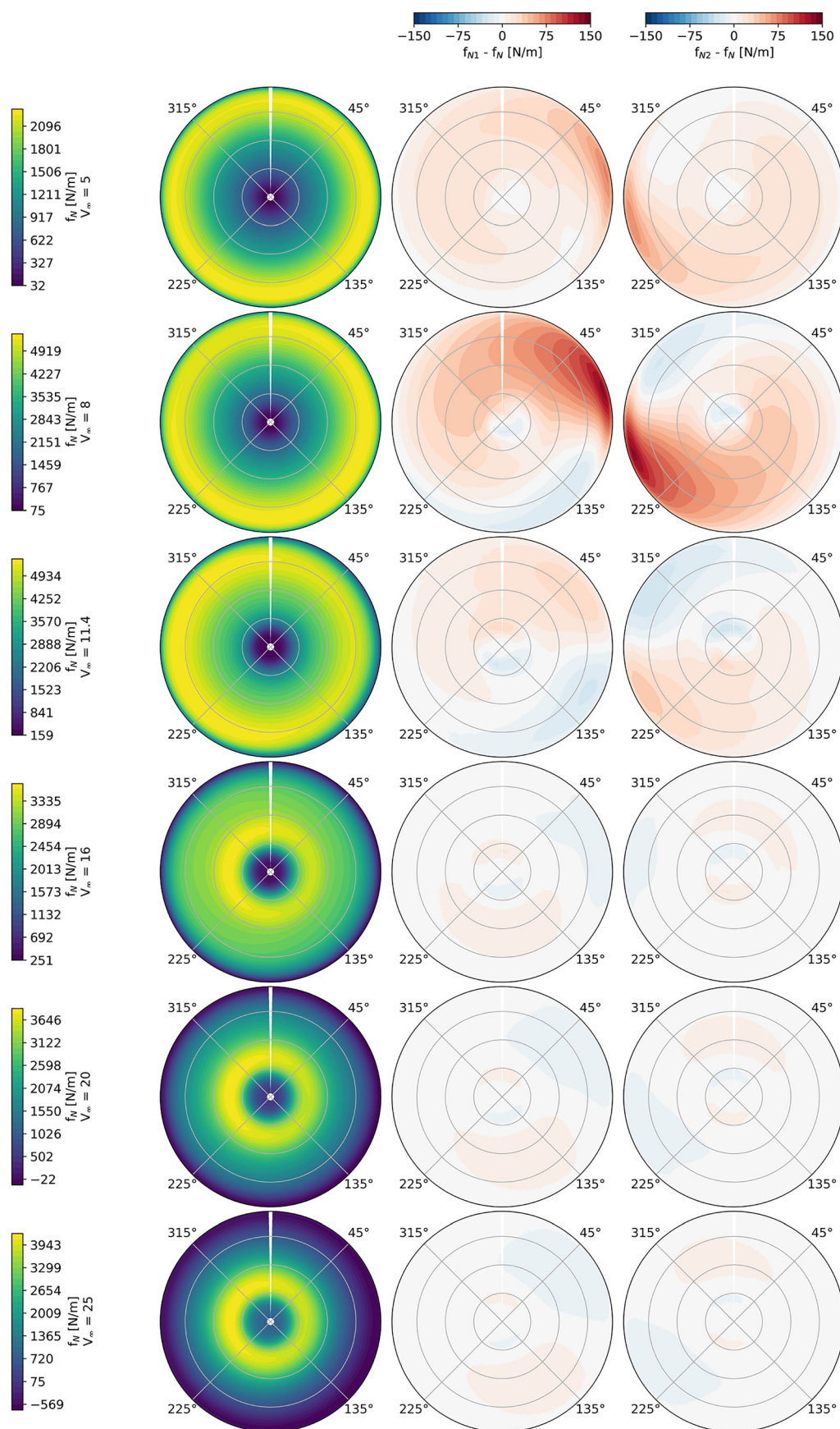
FIGURE 13 Normal forces per blade length for single configuration f_N (viridis) and its variation for the dual turbine configuration (blue/red) at different wind speeds.
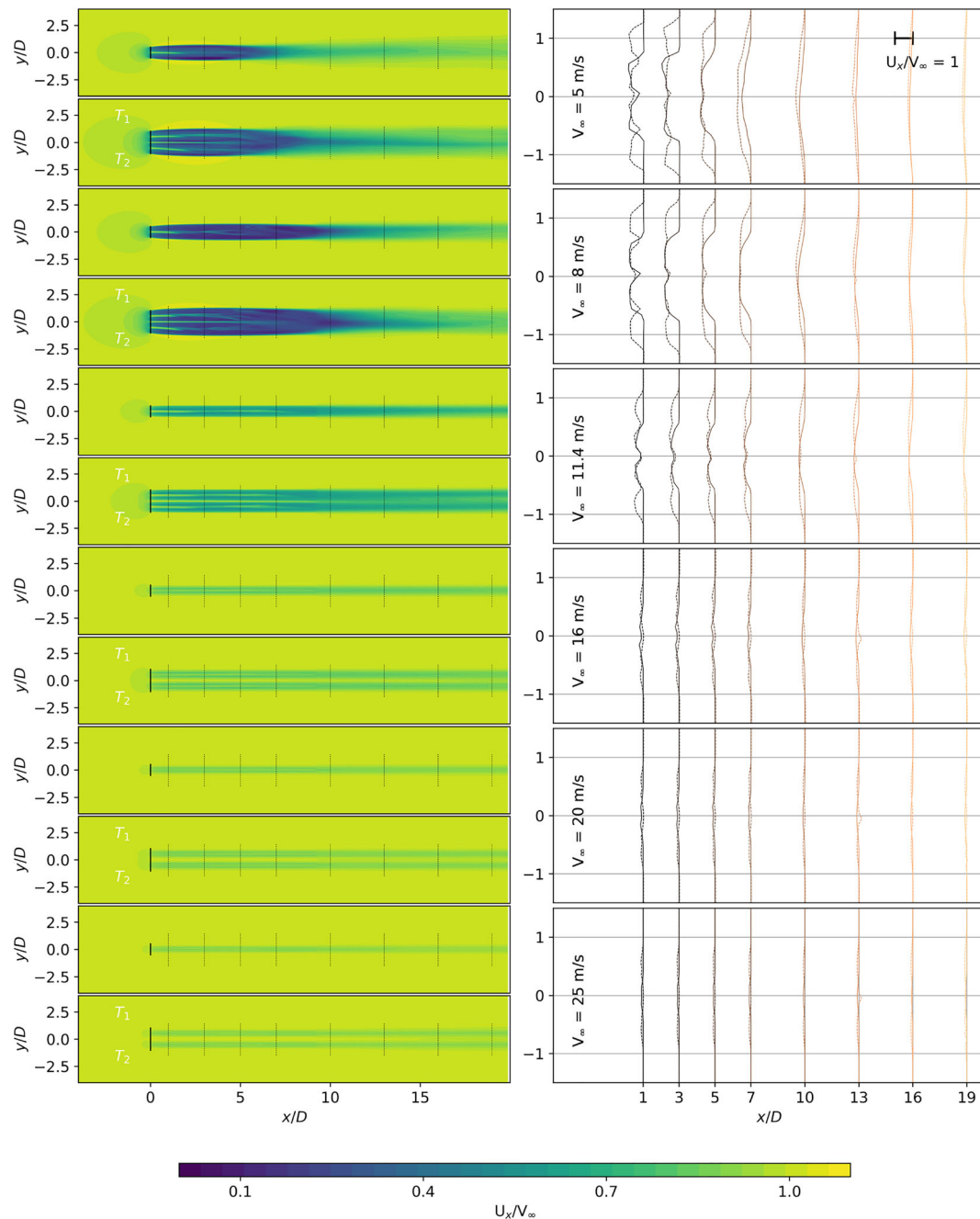
FIGURE 14 Normalized streamwise velocity component in the horizontal middle plane (left) with velocity profiles at different representative downstream sections (right) for different wind speeds. Continuous and dashed lines correspond to the single and dual rotor configuration, respectively.

configurations are close to negligible after seven diameters behind the turbines, a reference distance from which the next turbine could be positioned according to existing industry practices. Thus, the wake recovery is not affected along the streamwise wind direction by having the second closely spaced turbine.

Figure 16 depicts the streamwise turbulence intensity and Q-value isolines (of 0.0001) in the horizontal middle plane for both single and dual turbine configurations. At lower wind speeds, a higher turbulence intensity (and vortical structures) is observed for the dual turbine configuration. For the single turbine configuration, the vortical structures released from the rotor propagate downstream with the free-stream flow. For the dual turbine configuration, the vortices from each turbine actually merge early within the resulting wake thus increasing the turbulence intensity levels compared to that of a single turbine configuration. In general, larger turbulence levels lead to a faster wake recovery process due to the improvement of the mixing process as well as the momentum transfer.
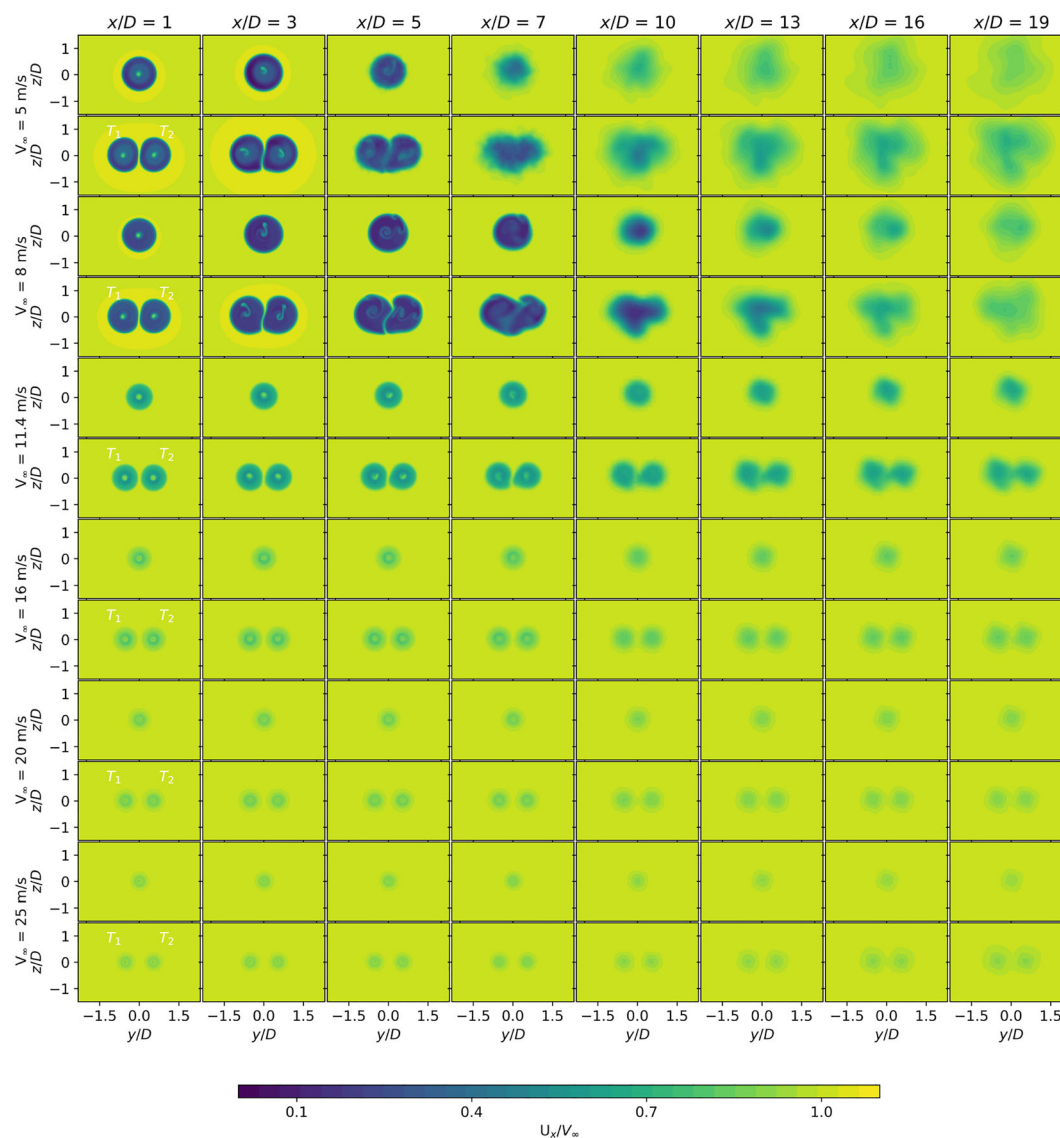
FIGURE 15 Normalized streamwise velocity component at different representative downstream sections for different wind speeds.
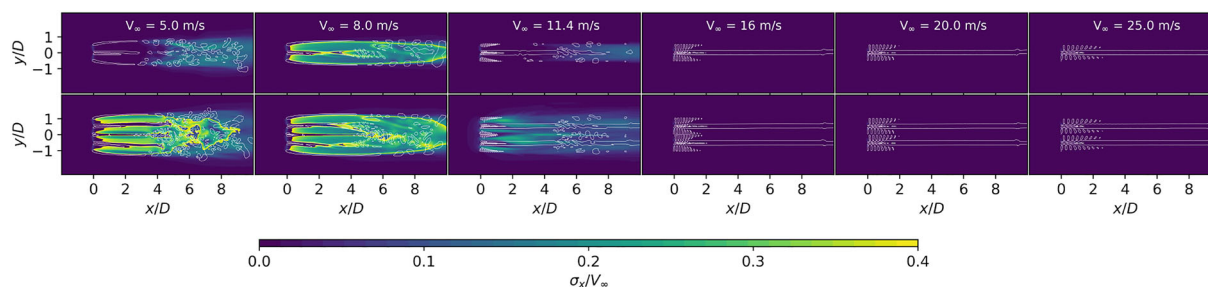

FIGURE 16 Streamwise turbulence intensity in the horizontal middle plane and isolines for a Q-value of 0.0001.

5 | CONCLUSIONS

The presented work has investigated the aerodynamic performance of the novel Hexicon TwinWind configuration, with a relatively close distance of 1.05D between the wind turbines. The influence of mesh resolution and domain size has been studied to verify the numerical model. The

validation of the aerodynamic performance of the numerical model has shown a good agreement with power and thrust data of the offshore 10-MW reference wind turbine.[13] The employed numerical model has thus been considered appropriate to assess the aerodynamic performance of the TwinWind and the single wind turbine configurations. The detailed assessment has been done for a wide range of operational wind speeds. Blade loads and the general wake structure of the two configurations have been studied at different operational wind speeds.

The reference turbine has a slightly better aerodynamic performance within the dual configuration, and this improvement is more evident at lower wind speeds (higher aerodynamic power of approximately 2% to 3% per turbine).

The dual configuration does not present relevant differences either in terms of the blade loads fluctuations or their magnitude compared to the single turbine for all blade positions within one revolution, thus eliminating potential concerns related to design blade limits and fatigue. The largest difference of the tangential and normal root bending moments are approximately 3% and 2%, respectively. The wake structure of the dual configuration is characterized by flow acceleration regions around and between the rotors, with a larger velocity deficit area close to the turbines as well as increased levels of turbulence intensity. The magnitudes of the velocity deficit profiles far downstream of the rotor (after 7D) are similar to the ones of the single turbine configuration. This indicates a comparable length of the wake recovery for both configurations. The results are consistent with ones obtained from authors of similar studies which consider multirotor concepts (with four and seven rotors), citations for which are provided in Section 1. This work has identified and quantified the beneficial features of multirotor concepts related to extra power and a faster wake recovery process, showing that they are also present for a configuration with only two turbines.

ACKNOWLEDGEMENTS

PEER REVIEW

The peer review history for this article is available at https://publons.com/publon/10.1002/we.2813.

DATA AVAILABILITY STATEMENT

The data that support the findings of this study are available on request from the corresponding author. The data are not publicly available due to privacy or ethical restrictions.

ORCID

Victor Mendoza https://orcid.org/0000-0001-5006-9231
Eirini Katsidoniotaki https://orcid.org/0000-0001-5096-3559

REFERENCES

1. Paulsen US, Pedersen TF, Madsen HA, et al. Deepwind—an innovative wind turbine concept for offshore. In: European Wind Energy Association (EWEA); 2011.
2. Commission E. *Energy Roadmap 2050*: Publications Office of the European Union; 2012.
3. Beiter PC, Tian T, Nunemaker J, et al. 2017 offshore wind technologies market update, National Renewable Energy Lab.(NREL), Golden, CO (United States); 2018.
4. Mendoza V, Goude A. Improving farm efficiency of interacting vertical-axis wind turbines through wake deflection using pitched struts. *Wind Energy*. 2019;22(4):538-546.
5. Laan MP, Andersen SJ, Ramos García N, et al. Power curve and wake analyses of the Vestas multi-rotor demonstrator. *Wind Energy Sci*. 2019;4(2): 251-271.
6. Hebbar U, Rane JD, Gandhi F, Sahni O. Analysis of interactional aerodynamics in multi-rotor wind turbines using large eddy simulations AIAA Scitech 2020 Forum; 2020:1489.
7. Speakman GA, Abkar M, Martínez-Tossas LA, Bastankhah M. Wake steering of multirotor wind turbines. *Wind Energy*. 2021;24(11):1294-1314.
8. W2power - combining wind and wave power to meet the energy demands of tomorrow. http://www.pelagicpower.no/about.html. Accessed: 2021-06-2.
9. Flow Concept. https://flowocean.com/flowconcept/. Accessed: 2021-06-26.
10. Chasapogiannis P, Prospathopoulos JM, Voutsinas SG, Chaviaropoulos TK. *Analysis of the aerodynamic performance of the multi-rotor concept*, Vol. 524; IOP Publishing; 2014;012084.
11. van der Laan MP, Abkar M. *Improved Energy Production of Multi-rotor Wind Farms*, Vol. 1256: IOP Publishing; 2019;012011.
12. Bastankhah M, Abkar M. Multirotor wind turbine wakes. *Physics of Fluids*. 2019;31(8):085106.
13. Bortolotti P, Tarres HC, Dykes K, et al. IEA wind task 37 on systems engineering in wind energy—WP2.1 reference wind turbines, International Energy Agency; 2019.
14. Sørensen JN, Shen WZ. Computation of wind turbine wakes using combined Navier-Stokes/actuator-line methodology. In: 1999 European Wind Energy Conference and Exhibition; 1999:156-159.
15. Bachant P, Wosnik M. Simulating wind and marine hydrokinetic turbines with actuator lines in rans and les. In: Aps division of fluid dynamics meeting abstracts; 2015:E28-003.

16. Bachant P, Goude A, Wosnik M. Actuator line modeling of vertical-axis turbines. arXiv preprint arXiv:1605.01449; 2016.

17. Bachant P, Goude A, Wosnik M. turbinesFoam: v0.0.7. https://doi.org/10.5281/zenodo.49422; 2016.

18. Mendoza V, Bachant P, Wosnik M, Goude A. Validation of an actuator line model coupled to a dynamic stall model for pitching motions characteristic to vertical axis turbines, Vol. 753 IOP Publishing; 2016:022043.

19. Mendoza V, Bachant P, Ferreira C, Goude A. Near-wake flow simulation of a vertical axis turbine using an actuator line model. *Wind Energy*. 2019; 22(2):171-188.

20. Mendoza V, Chaudhari A, Goude A. Performance and wake comparison of horizontal and vertical axis wind turbines under varying surface roughness conditions. *Wind Energy*. 2019;22(4):458-472.

21. Mendoza V, Goude A. Validation of actuator line and vortex models using normal forces measurements of a straight-bladed vertical axis wind turbine. *Energies*. 2020;13(3):511.

22. Mendoza V, Goude A. *Wake Flow Simulation of a Vertical Axis Wind Turbine Under the Influence of Wind Shear*, Vol. 854: IOP Publishing; 2017;012031.

23. Smagorinsky J. General circulation experiments with the primitive equations: I. The basic experiment. *Mon Weather Rev*. 1963;91(3):99-164.

24. Glauert H. Airplane propellers. *Aerodynamic Theory*: Springer; 1935:169-360.

25. Twinwind concept. https://hexicon.eu/twinwind/. Accessed: 2022-02-09.

26. Roache PJ. *Fundamentals of Verification and Validation*: Hermosa Publ.; 2009.

27. Eça L, Hoekstra M. A procedure for the estimation of the numerical uncertainty of CFD calculations based on grid refinement studies. *J Comput Phys*. 2014;262:104-130.

28. Hansen MH. Aeroelastic stability analysis of wind turbines using an eigenvalue approach. *Wind Energy: Int J Prog Appl Wind Power Convers Technol*. 2004;7(2):133-143.